1   **Title:**

2   **Wintertime lake drainage cascade triggers large-scale ice flow response in Greenland**

3

4   **Authors:**

5   **Nathan Maier[1,2]*, Jonas Kvist Andersen[3], Jérémie Mouginot[1,4], Florent Gimbert[1] and Olivier Gagliardini[1]**

6

7   **Affiliations:**

8   [1]Univ. Grenoble Alpes, CNRS, IRD, Grenoble INP, IGE, 38000 Grenoble, France

9   [2]Los Alamos National Lab, Los Alamos, NM 87544,USA

10   [3]DTU Space, Tech. Univ. of Denmark, 2800 Kgs. Lyngby, Denmark

11   [4]Depart. of Earth System Science, Univ. of California- Irvine, Irvine CA 92697, USA

12   *Corresponding Author Email: ntmaier@gmail.com

13

14   **Abstract:**

15   Surface melt forces summertime ice-flow accelerations on glaciers and ice sheets. Here, we show that

16   large meltwater-forced accelerations also occur in winter in Greenland. We document supraglacial lakes

17   (SGLs) draining in cascades at unusually high elevation, causing an expansive flow acceleration over a

18   ~5200 km^2 region during winter. The 3-component interferometric surface velocity field and

19   decomposition modeling reveals the underlying flood propagation with unprecedented detail as it

20   traveled over 160 km from the drainage site to the margin, providing novel constraints on subglacial water

21   pathways, drainage morphology, and links with basal sliding. The triggering SGLs continuously grew over

22   40 years and suddenly released decades of stored meltwater into regions of the bed never previously

23   forced, demonstrating surface melt can impact dynamics well beyond its production. We show these

24   events are common and thus their cumulative impact on dynamics should be further evaluated.

25   **Plain language summary:**

26   Understanding factors that influence flow speeds on ice sheets is linked to our ability to predict changes

27   in sea level and prepare coastal communities for the future. In Greenland, ice flow-speed changes have

28   long been linked to surface melting in summer. Meltwater can make it to the bed of the ice sheet via

29 surface cracks causing changes in ice motion. Here, we show that melt that is produced during summer,

30 but stored within lakes on the ice surface, can drain to the bed and cause large flow accelerations during

31 winter. This demonstrates the influence of meltwater on flow speeds needs to be considered beyond

32 when it is produced.

33 **Key points:**

34 • A cascade of supraglacial lake drainages and an associated acceleration in ice flow are observed

35   during winter in Greenland.

36 • Decomposition of motion into vertical and horizontal components allows for subglacial water

37   pathways and links with sliding to be inferred.

38 • Tracking the history of the supraglacial lakes shows some of the meltwater released was

39   produced decades earlier.

40 **1 Introduction**

41 The annual velocity cycle along the margins of Greenland is closely linked to meltwater availability

42 (Andrews et al., 2018; Bartholomew et al., 2010; M. Hoffman et al., 2011; Sole et al., 2013; Van de Wal et

43 al., 2015). In early summer, the ice sheet accelerates as surface meltwater is delivered to the bed and is

44 routed through an inefficient subglacial drainage system favoring high basal water pressures (Andrews et

45 al., 2018; Bartholomew et al., 2010; M. Hoffman et al., 2011). In late summer, drainage efficiency gains

46 cause water pressures to decrease, decelerating the ice sheet back to or below the previous winter values

47 (Andrews et al., 2018; Bartholomew et al., 2010; M. Hoffman et al., 2011; Sole et al., 2013; Van de Wal et

48 al., 2015). In the absence of surface melt during the winter period, flow speed typically follows a

49 monotonic increase (Harper et al., 2021; Van de Wal et al., 2015), which is attributed to decreasing ice-

50 bed coupling from in situ production of basal melt (Harper et al., 2021). This cycle is the basis of current

51 understanding of hydrology-dynamic coupling and how increased melting will influence flow speeds and

52 mass loss in the future (Davison et al., 2019).

53 Large transient changes in surface velocities are typically not expected during winter due to the absence

54 of surface melt. Yet, perennial water storage of the previous summer's meltwater can occur within

55 supraglacial lakes (SGLs) that remain partially unfrozen through winter (Benedek & Willis, 2021; Koenig et

56 al., 2015; Lampkin et al., 2020; Law et al., 2020; Schröder et al., 2020). Recent work indicates isolated

57 lakes can drain during winter (Benedek & Willis, 2021; Schröder et al., 2020), but current evidence does

58 not suggest a significant impact on flow speeds (Benedek & Willis, 2021). This contrasts to observations

59 made during summer, where SGL drainages, and particularly drainage clusters, can drive multi-day

60 accelerations across large areas due to the friction reduction as the rapid influx of water to the bed drains

61 downgradient (Andrews et al., 2018; Christoffersen et al., 2018; M. J. Hoffman et al., 2018; Mejía et al.,

62 2021).

63 Here, we document a cascading lake drainage that generates an expansive flow acceleration wave during

64 winter in western Greenland (*Fig. 1*). We decompose the motion into its horizontal and vertical

65 component and perform surface deformation modeling to determine likely flow pathways and drainage

66 characteristics as the flood wave propagates to the margin. Finally, we document the historical SGL growth

67 that enabled the incipient drainages, hypothesize triggering mechanisms, and put dynamic impact in the

68 context of long-term change.

69 **2 Methods**

70 **2.1 DInSAR Velocities**

71 We use Sentinel-1 image pairs with a 6-day temporal baseline from three tracks (T90, T25, and T127) to

72 generate line-of-sight (LoS) velocity maps before, during, and after the lake drainages following the

73 approach outlined in (Andersen et al., 2020) and (Kusk et al., 2021). Velocities were derived using

74 differential SAR Interferometry (DInSAR), which exploits the difference in phase signal between

75 subsequent acquisitions. Although DInSAR only retrieves a single component of the velocity vector and is

76 limited to regions in which interferometric coherence is retained, the measurement accuracy and spatial

77 resolution is significantly higher (~0.5 m/y vs. tens of m/y difference in accuracy, order of magnitude

78 higher spatial resolution) than that obtained with tracking-based measurements (Andersen et al., 2020) .

79 **2.2 Identifying Winter Lake Drainages**

80 We manually identified 15 winter supraglacial lake drainages during March of 2018 using all Sentinel-2

81 (ESA) and Landsat 8 (USGS) optical imagery acquired for the region between February 15th and April 29th,

82 2018. The frozen lake surfaces are near roughness-free, making them readily identifiable from

83 surrounding regions (*Fig. S1*). Lake drainages are identified via the abrupt change from smooth surfaces

84 to collapse basins or rough lakebeds from scene to scene. We interpret this to result from the loss of

85 mechanical support provided by the underlying water, indicating drainage or partial drainage of the lake

86 below the ice lid via hydrofracture. Similar surface features and interpretation were used to confirm

87 winter drainage detection using other methods (Benedek & Willis, 2021; Schröder et al., 2020).

2.3 Decomposing Vertical and Horizontal Motion

We exploit the fact that DInSAR measurements are sensitive to both horizontal and vertical motion to decompose the velocity into vertical and horizontal components for select time periods during the drainage event. Estimating the three-dimensional velocity vector requires three spatiotemporally overlapping tracks with different viewing geometries. The satellite coverage does not allow this, and we instead use data from one ascending and one descending Sentinel-1 track (T90 and T25) to estimate two components of the velocity: horizontal speed in the flow direction, u_{FD}, and vertical speed, u_v. We use the PROMICE average velocity map (2016-2019) (Solgaard et al., 2021) to constrain the flow direction and assume it remains constant during the event. The measured LoS motion from each track can then be decomposed using a system of equations:

$$u_{LoS,asc} = cos\ \alpha_{asc}\ cos\ \theta_{asc}\ u_{FD} + sin\ \theta_{asc}\ u_v \qquad (1a)$$

$$u_{LoS,dsc} = cos\ \alpha_{dsc}\ cos\ \theta_{dsc}\ u_{FD} + sin\ \theta_{dsc}\ u_v \qquad (1b)$$

where $\alpha = \beta - \phi$ is the angle between the horizontal flow angle, β, and the ground-projected radar LoS (described by the angle φ), and is the elevation angle between the LoS and its ground projection. We use eqs. (1a-b) to solve for the two unknowns, u_{FD} and u_v. The temporal overlap between the chosen tracks is 4.5 days, meaning that some uncertainty is added by the fact that the two measurement periods do not perfectly overlap. Given the relatively slow velocity of the propagating wave (<0.1 m/s), we expect the displacement to be similar between image scenes. We test this assumption and our inference of uplift by decomposing a synthetic wave model constrained by the observations (*section 2.4*).

To reduce the noise from spatially correlated errors specific to each track, we estimate the change in, rather than absolute velocities resulting from the drainage event. Hence, eqs. (1a-b) become:

$$du_{LoS,asc} = cos\ \alpha_{asc}\ cos\ \theta_{asc}\ du_{FD} + sin\ \theta_{asc}\ du_v \qquad (2a)$$

$$du_{LoS,dsc} = cos\ \alpha_{dsc}\ cos\ \theta_{dsc}\ du_{FD} + sin\ \theta_{dsc}\ du_v \qquad (2b)$$

where du_{LoS} is the difference between the measured LoS velocity field and a reference field (taken as a DInSAR LoS measurement from the same track prior to the SGL drainages).

118

2.4 Synthetic Wave Model

120   To evaluate how the assumptions made to decompose the LoS velocities may bias the retrieved horizontal

121   and vertical velocity fields, we decompose a synthetic coupled horizontal and vertical displacement wave

122   using the same procedure as described in section 2.3 for the observed data. We model a coupled

123   horizontal and vertical flowline velocity wave, which mimics a horizontal flow increase driven by bed

124   separation, as gaussian kernels propagating across a 160 km flowline using a kernel width (σ) and wave

125   speed constrained by our data. We then calculate the accumulated horizontal displacement and change

126   in uplift that would occur between the two 6-day windows that overlap by 4.5 days to match the interval

127   between the T90 and T25 orbital tracks. Finally, we decompose the signal using the mean orbital

128   parameters from the T90 and T25 tracks and compare the results to the decomposed fields to constrain

129   the conditions required to reproduce the major features of the data.

3. Results and Discussion

3.1 Wintertime Lake Drainage Cascade

132   On approximately March 9th 2018, two SGLs drained in a land terminating sector just south of Jakobshavn

133   Isbræ 142 km inland from the westernmost ice margin and at high elevations (~1600 m) (*Fig. 1, S1*). This

134   altitude corresponds to the multi-year snowline (Vandecrux et al., 2019), which approximates the

135   transition between the accumulation and ablation zones. Before the event, no observable acceleration is

136   detected. These incipient drainages trigger an acceleration in the direct vicinity of the draining lakes

137   marking the initiation of a marginally propagating velocity wave.

138   Between March 9th and 12th, eight additional lakes drained ~40 km downstream and ~20 km north of the

139   original drainage cluster (*Fig. 1E, S1*). During this period, LoS velocities increase up to 160% of pre-drainage

140   values. The wave exhibits a complex structure and bifurcates into two main paths. The wave heading west

141   propagates towards Nordenskiöld Glacier, a relatively slow-moving outlet glacier (~200 m/yr). This

142   western path shows multiple branches emanating from the northern and southern part of the original

143   drainage cluster that coalesce downglacier later on. The wave heading north propagates towards

144   Jakobshavn Isbræ, the fastest marine-terminating outlet glacier in Greenland (>10 km/yr), along a single

145   branch (*Fig. 1*). The velocity branches always closely follow the troughs in the bed topography.

146   As the event continues, the westward wave front continues to move downglacier and again shows a

147   complex multi-branched structure following bed depressions (*Fig. 1F*). The northernmost wave front is no

148 longer clearly visible, extending beyond the usable DInSAR observations. The westward branches

149 eventually coalesce ~80 km downglacier from the original drainage site. LoS velocities within the main

150 wave remain 160% of their background value. Between March 18th and 24th, the westward wave front

151 enters the main Nordenskiöld trough, and velocities increase to ~250% above background (*Fig. 1G*).

152 Between March 24th and 30th, three more SGLs are observed to drain about 60 km upglacier of the wave

153 front (*Fig. 1H*). This drainage causes an additional acceleration following an angular bed trough to the

154 north which rejoins the main wave path before entering the Nordenskiöld bed trough. The wave front

155 reaches the terminus of Nordenskiöld between March 30th and April 4th, ~25 days after its initiation. This

156 timing coincides with the proglacial release of water from Nordenskiöld proglacial delta observed in

157 optical imagery (*Fig. S2*).

158 **3.2 Drainage Characteristics Revealed by Decomposition of the Velocity Field**

159 Using the approach outlined in 2.3, we invert for horizontal motion (relative to pre-drainage velocities)

160 and the vertical displacement and find they exhibit strikingly distinct patterns (*Fig. 2, S3*). The horizontal

161 velocity field is smooth and spatially extends over 10-50 km in flow-perpendicular width, while the uplift

162 is concentrated in a bead and thread structure with a characteristic width of <10 km, where high uplift

163 patches (~0.25 m) are linked together through thinner uplift connectors of lower amplitude.

164 Synthetic modeling validates the decomposition assumptions and the interpretation that the decomposed

165 fields mainly represent horizontal and vertical motion (*Fig. 2*; *section 2.4*). We find the best fit to the

166 decomposed data is a horizontal (amplitude = 60 m/yr) and vertical uplift/bed separation wave (amplitude

167 = 0.25 m) propagating at 0.08 m/s, all values within the constraints of the data. This fit indicates the

168 horizontal velocity wave is wider (σ = 15 km) and precedes the uplift wave (σ = 10 km) by 15 km. These

169 parameters capture the phase relationship between the peaks as well as the pre- and post-wave dips in

170 vertical displacement observed in the decomposed fields. The phase difference between the decomposed

171 and synthetic waves, as well as the pre-wave dip in vertical displacement indicates the fields are

172 somewhat distorted compared to the original values due to the mismatch in temporal overlap. However,

173 we still find we can clearly distinguish horizontal motion and vertical displacement, allowing us to infer

174 vertical and horizontal fields from the decomposed data shown in *Fig. 2a*.

175 Following the results of the modeling, we interpret the uplift, which produces the complex structure in

176 *Fig. 1,* as changes in bed separation that identify likely flow pathways (*Fig. 2, S4, SI*) as the ~0.18 km[3] of

177 meltwater (*SI*) injected into the ice-bed interface drains towards the margin. This is supported by the

178   following evidence: (i) neither vertical motion resulting from vertical strain or bed tangential motion are

179   likely to produce such a pattern (*Fig. S5*); (ii) the uplifted branches correspond to hydropotential lows

180   within the bed troughs, which is the expected pathway of subglacially draining water (*Fig. 1A, S6*); (iii)

181   regions of highest uplift correspond to depressions in the hydropotential (subglacial sinks) (*Fig. S7*). The

182   bead and thread uplift structure suggests a fill and spill drainage style similar to the drainage of subglacial

183   lakes (Dow et al., 2016; Livingstone et al., 2016), with water captured by each sink along the flow path is

184   released when the pressure reaches the hydropotential lip of each depression. Drainage through these

185   regions requires overpressure, which can physically cause bed separation either due to the detachment

186   of the ice base via floatation or upward cavity formation via ice creep (Andrews et al., 2018; Bartholomaus

187   et al., 2008; Bartholomew et al., 2010; Cowton et al., 2016; Gagliardini et al., 2007; Helanow et al., 2021;

188   M. Hoffman et al., 2011), and is thus consistent with the beads of high uplift (*Fig. 2, S7*).

189   The comparatively smooth and expansive extent of the horizontal field indicates much of the horizontal

190   acceleration is not directly related to bed separation. We posit that the changes in bed friction are linked

191   to bed separation as conceptualized by (Gagliardini et al., 2007; Gilbert et al., 2022; Gimbert et al., 2021;

192   Schoof, 2005; Tsai et al., 2022) and more expansive changes in dynamics occur through stress transmission

193   within the ice - a behavior inferred previously from scarce in situ measurement and modeling (Andrews

194   et al., 2014; Derkacheva et al., 2021; M. J. Hoffman et al., 2016; Maier et al., 2021; Ryser et al., 2014) but

195   never documented observationally. Alternatively changes in bed friction could be generated via water

196   pressure increases emanating beyond the uplifted region. We suggest this scenario is less likely given

197   subglacial observations show pressure communication typically occurs only across short distances

198   (Andrews et al., 2014; Rada & Schoof, 2018).

199   We estimate the speed of the velocity wave that propagates along the interpreted main Nordenskiöld

200   drainage pathway (*Fig. S4*) to be between 0.03-0.17 m s^{-1} (*Fig. 3, SI*). This velocity is consistent with repeat

201   dye tracer experiments in Greenland which show seasonally evolving drainage velocities which increase

202   ~0.1 m/s to ~1 m/s as the melt season progresses (Chandler et al., 2013). This increase was inferred to

203   reflect the transition from inefficient to efficient drainage pathways. Our event-averaged drainage

204   velocity of ~0.1 m/s and 1-10 km scale of the uplifted regions would imply drainage mainly through

205   inefficient and distributed drainage pathways rather than through channelized or turbulent sheet

206   components where drainage speeds are expected to be >1 m/s (Chandler et al., 2013; Tsai & Rice,

207   2010). Even so, given the spatiotemporal integrated nature of the velocities and varying hydropotential

208   gradient, it is plausible many drainage styles could have manifested at some point along the drainage

209 path. The drainage speed slows to about 0.05 m/s as the water enters the Nordenskiöld trough while

210 horizontal velocities increase by 250% even though modeled hydropotential gradients are high and no

211 modeled subglacial sinks are present *(Fig. 3)*. This implies the drainage system conductivity is lower within

212 the trough possibly due to the accumulation of sediments, where water drains mainly via Darcian flow, or

213 to differences in the pre-existing drainage system geometry.

214 **3.3 Hypothesized Trigger Mechanisms**

215 In the absence of surface melting, which can cause SGL overspill, the drainages likely occur due to

216 hydrofracture to the ice base (Chudley et al., 2019; Das et al., 2008; Stevens et al., 2015). The initial

217 formation of crevasses necessary for hydrofracture requires precursor events that generate tensile stress

218 transients (Christoffersen et al., 2018; Stevens et al., 2015). Here, no precursor is directly observed (*Fig.*

219 *1*), however it is possible that a short duration event would not be detected in our six-day velocity maps.

220 Yet, the initially draining lakes are located near the snowline (*Fig. 1*), and are far inland from the terminus

221 of any outlet glacier, which would be the most likely place for large transients to originate during

222 winter. Given this, we suggest several other plausible ways the incipient drainage could occur: (i) a stress

223 transient and surface fracture could have occurred due to a local stick-slip event or a subglacially migrating

224 water body; (ii) an upgradient crevasse could migrate into the SGL, negating the need for concurrent

225 crevasse formation; (iii) rapid cooling could thermally fractured the ice surface adjacent to the incipient

226 SGL (Podolskiy et al., 2019). Evaluating these hypotheses will ultimately require more detailed data than

227 is presented here.

228 Once the initial lake drainage has started, the resulting ice displacements can generate stress transients

229 that can trigger hydrofracture within nearby lakes (Christoffersen et al., 2018; Doyle et al., 2013; Tedesco

230 et al., 2013), thus initiating a cascade of SGL drainages near the original drainage location. Interestingly,

231 many drainages occur more than 40 km away from and up to 14 days after the original drainage. This

232 would indicate that their drainage is unrelated to stress transients related to ice-tectonic deformations

233 around the incipient drainages and are tapped after the velocity wave passes and tensile stress conditions

234 are favorable for hydrofracture.

235 **3.4 Decadal Scale-Storage and Release of Meltwater**

236 Tracking the evolution of the SGLs since 1972 to estimate the changes in their area through time (*Fig. 4,*

237 *S10*) reveals many of these lakes formed and grew for years to decades before initially draining, and for

238 the two of the highest elevation lakes (Lake 1 and 3), this was the first observed instance of drainage after

239   a half century of growth (*Fig. 4*). This suggests that events like these, where high-elevation SGLs drain and
240   trigger an expansive downgradient acceleration, are linked to increases in melt production which promote
241   the formation and growth of high elevation lakes (Leeson et al., 2015). The historical lake evolution
242   records (*Fig. 4, S8*) also show that once drained, lakes appear to drain more frequently thereafter;
243   indicating initial SGL drainage might play a role in establishing persistent surface-to-bed connections
244   where there were none prior.

245   **3.5 Implications for Long-term Ice Flow**

246   Recent work suggests persistent basal water storage has a prominent role in long-term evolution of
247   Greenland (Maier et al., 2022). Although well-studied (Davison et al., 2019), the specifics of how and when
248   water is stored at the base remains elusive. Here, we show melt-forced coupling changes can occur during
249   winter, which for this event increases annual ice discharge by 1-4% (*Fig. S9, SI*) compared to if the event
250   did not occur. Further, flow velocities before and after the flood wave passes shows regions around the
251   drainage pathway have slowed upstream of the Nordenskiöld by 5-10% while within the Nordenskiöld
252   they have increased by 10-20% (*Fig. 1J*), implying commensurate changes in subglacial water storage due
253   to the passing of the subglacial flood. These factors suggest events like these have the potential to impact
254   multi-annual velocity variability and could potentially precondition the drainage system for the following
255   summer and have a broader impact on dynamics in a way not resolved in this analysis. Yet, given the
256   spatiotemporally isolated nature of the event and modest impact on ice flow, events like these would
257   have to occur frequently to have a substantial impact on marginal dynamics. Undertaking a precursory
258   search in the vicinity of Nordenskiöld glacier during the following years (2019-2021), we identified four
259   additional winter drainage events with associated dynamic changes (*Fig. S10, S11*), suggesting wintertime
260   transients are common along the margins of the ice sheet and necessitate further study to assess their
261   cumulative impact.

262   **4 Conclusion**

263   Our finding links expansive flow changes during winter to summer meltwater production, demonstrating
264   surface melt can have a prolonged influence on dynamics that persists beyond when it is
265   generated. Moreover, we demonstrate this lag can be up to decades, meaning the hydrology-dynamic
266   cycle, which is usually considered on an annual and seasonal basis, can operate on fundamentally different
267   timescales. The unique winter timing and high-resolution nature of the data revealed drainage structure
268   and the link between uplift and sliding across scales not achievable via in situ studies. Thus, in addition to

269   establishing the impact of winter SGL drainages and triggering mechanisms, future work should seek to

270   leverage events like these to provide key constraints on hydrologically driven transient friction changes.

A

Bed elev. [km]
0.5
0.0
-0.5

B

Avg. speed [m/y]
10^4
10^3
500
200
100
10

C

11
7
6
14 13   12 10   5 2
15   9 8   4 3
                        1

2018/02/28 - 2018/03/06

D

2018/03/03 - 2018/03/09

E

2018/03/06 - 2018/03/12

F

2018/03/12 - 2018/03/18

G

2018/03/18 - 2018/03/24

H

2018/03/24 - 2018/03/30

I

2018/03/30 - 2018/04/05

J

2018/04/05 - 2018/04/11

25 km

LoS velocity
change [%]

-75   -50   -25   0   25   50   75
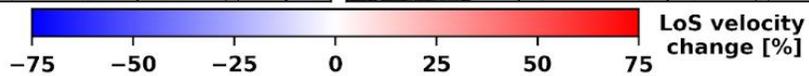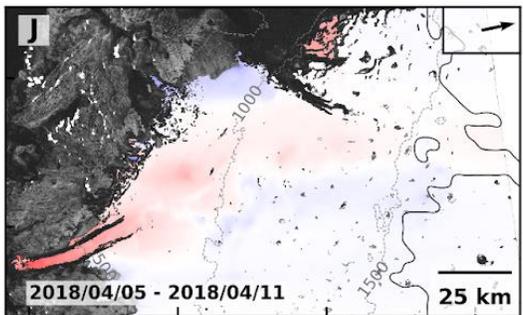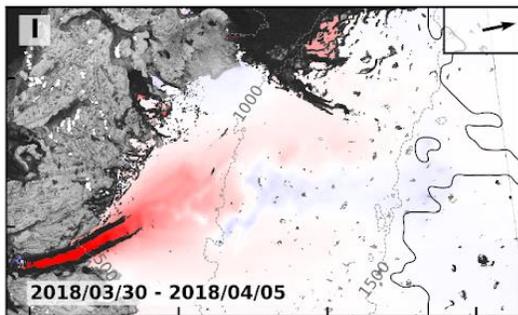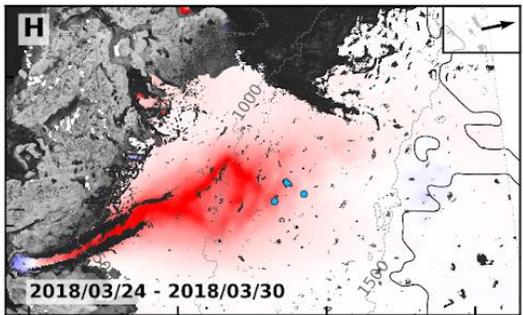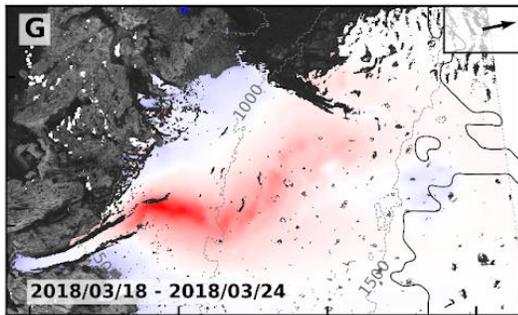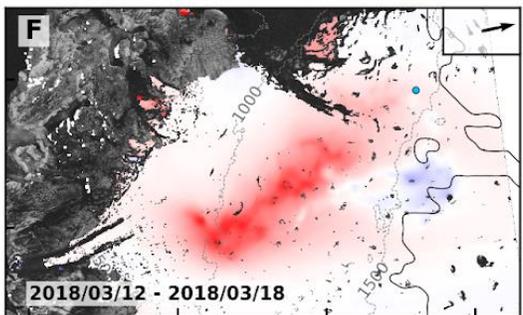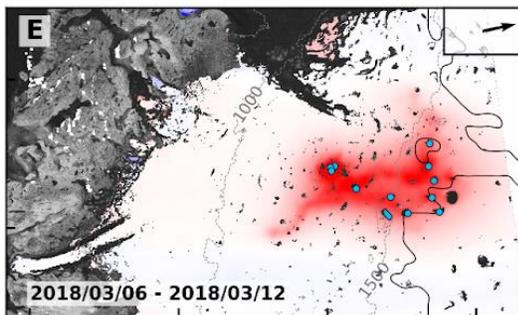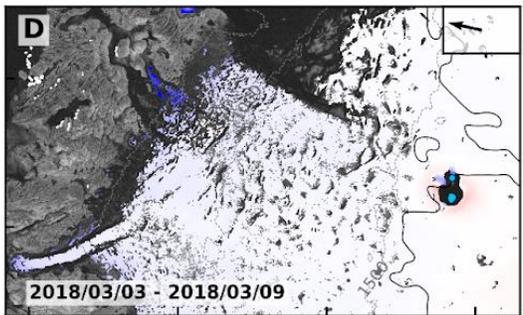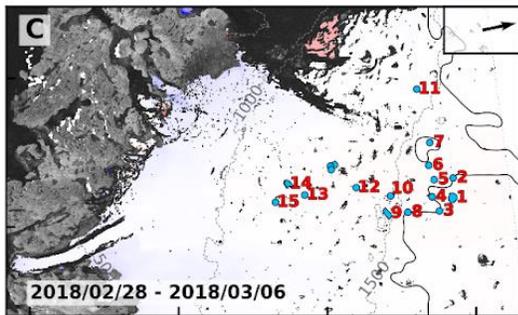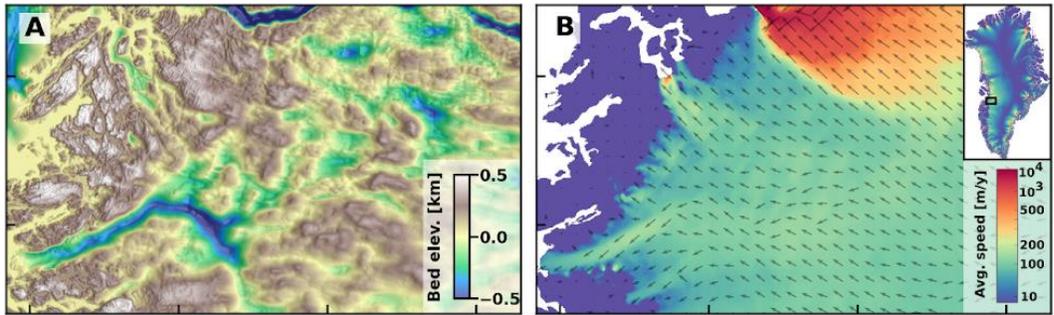
Figure 1 – Winter drainage cascade and dynamic response – Panels (**A**) and (**B**) show bed elevation (Morlighem, 2018; Morlighem et al., 2017) and 1995-2016 average velocity (Mouginot et al., 2019). Remaining panels show the change in line-of-sight velocity (relative to a pre-event acquisition) from Sentinel-1 interferometric (DInSAR) measurements (*section 2.1*) overlaid on corresponding coherence images. Panel (**C**) shows the location of all lakes inferred to have completely or partially drained (blue polygons, or dots for lakes smaller than 4 km^2) along with the velocity anomaly field pre-drainage. The following panels show the sequence of lake drainages and the propagation of the resulting velocity wave. Lakes appear when they are inferred to drain, coincident with the period of the velocity acquisition. Velocity changes are measured from Sentinel-1 tracks 90 (panels (**C**) and (**E**)-(**J**)) and 127 (panel (**D**)). The black arrow indicates ground-projected line-of-sight, dashed lines indicate surface elevation contours, and the solid line indicates the time-averaged snowline (Vandecrux et al., 2019).

A

Decomposition Period:
03/12/18 - 03/20/18

decomposed horizontal motion (m yr⁻¹)

20 km

B

interpreted drainage
pathways

decomposed vertical displacement (m)

C

vertical displacement (m)

horizontal velocity (m yr⁻¹)

decomposed

easting (m)

×10⁵

D

modeled

bed sep.   v. disp.   horiz.

inland distance (km)
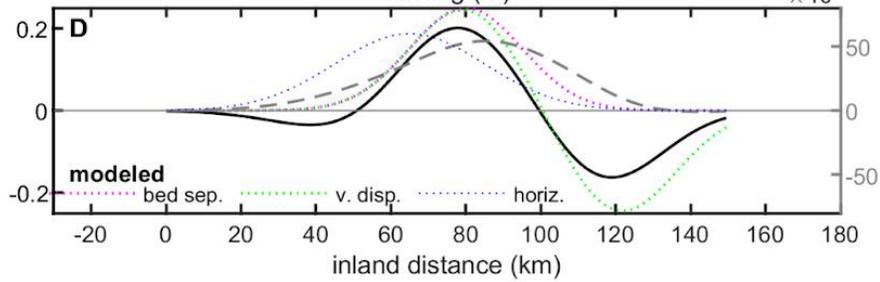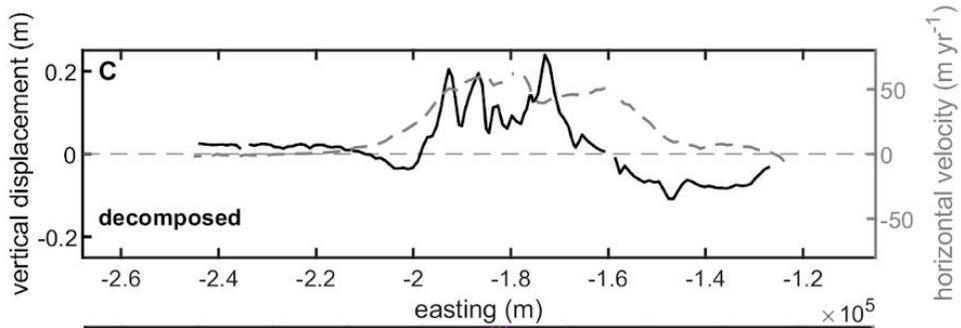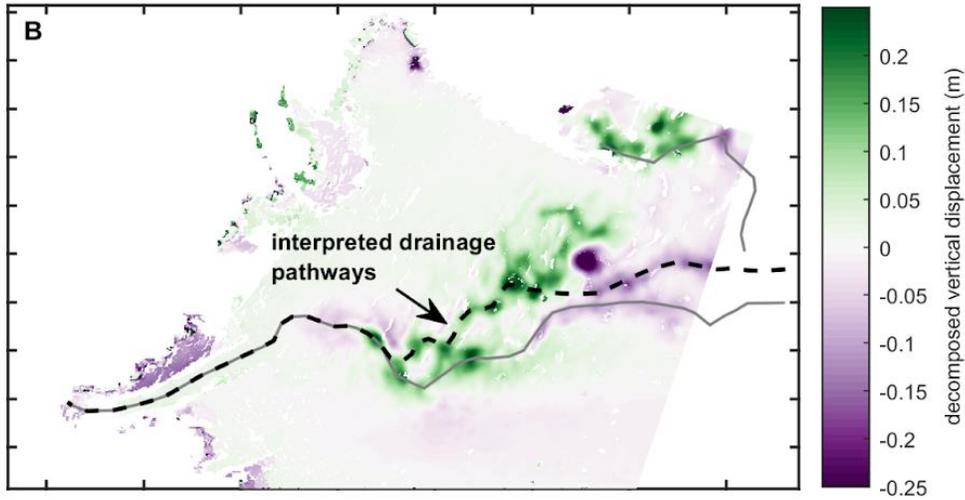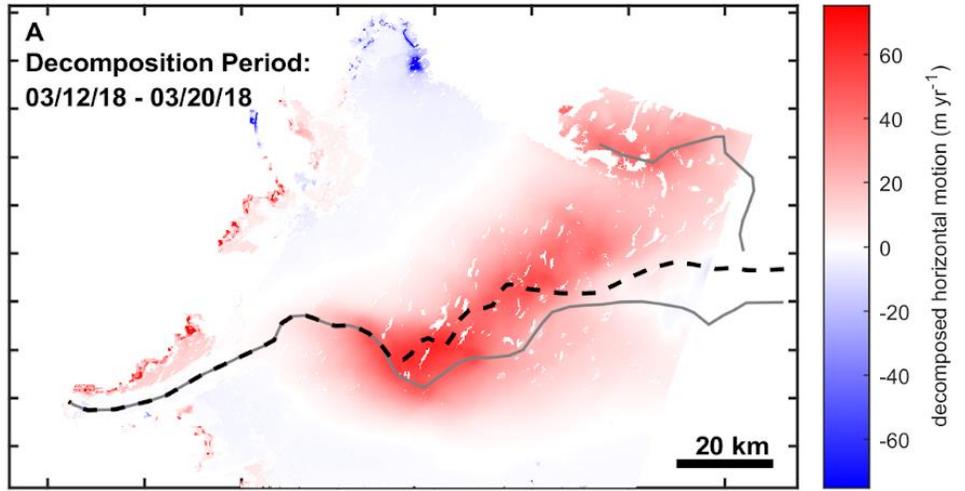
Figure 2 – Decomposed motion – Snapshot of decomposed horizontal motion (relative to pre-drainage velocities) (**A**) and vertical surface displacement (**B**) during drainage event. The three interpreted flow pathways are shown with solid gray and black dashed lines. **C.** Decomposed horizontal (gray dashed) and vertical (solid black) motion along the center flowline (dashed black line in panel **C**). **D**. Decomposition (horizontal motion - gray dashed, vertical displacement/change in uplift over 6-day window - solid black) of synthetic velocity wave (dotted blue) and uplift wave (dotted pink, vertical displacement - dotted green) with characteristics constrained by the data (*sections 2.3-2.4*).
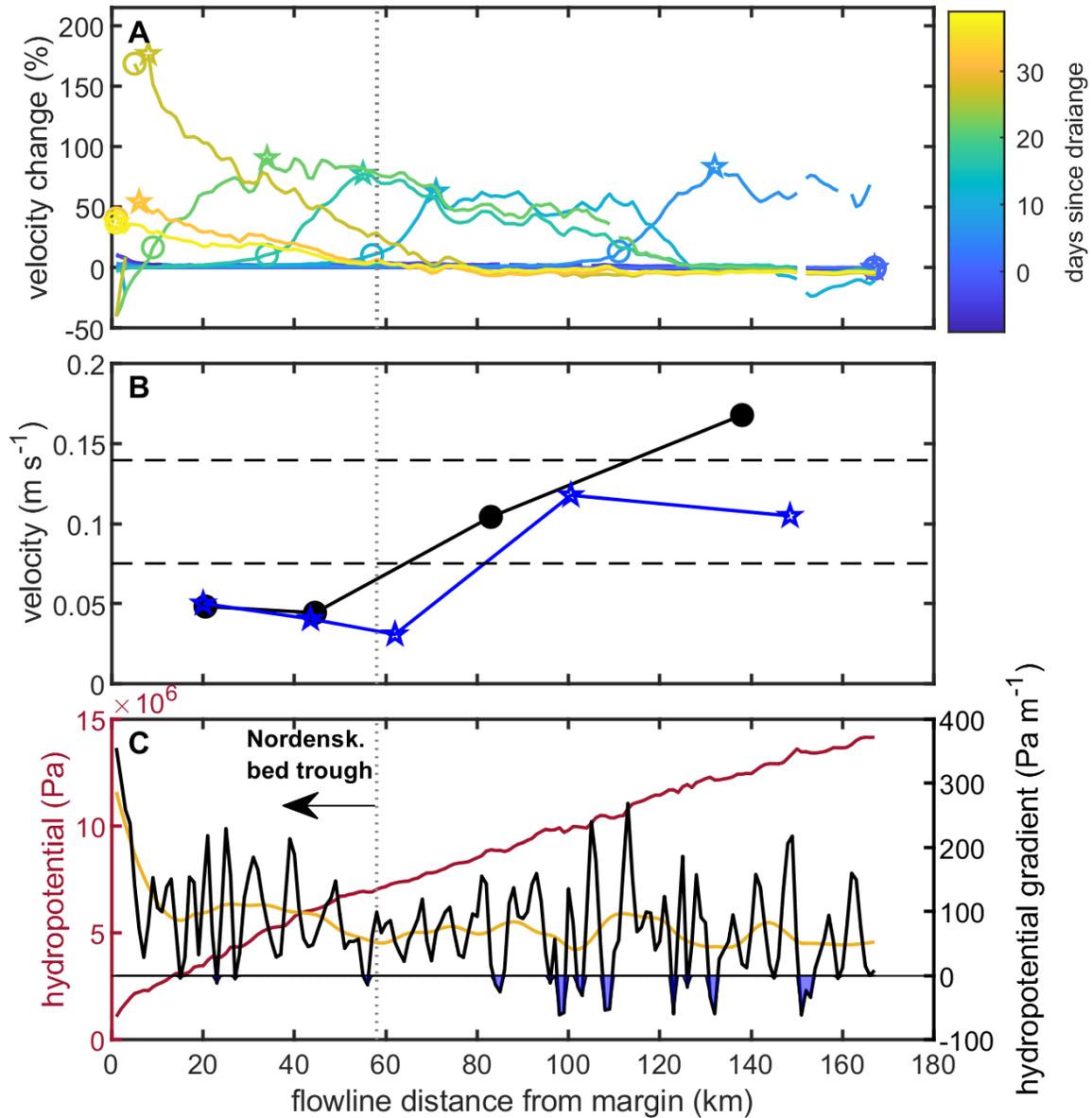
Figure 3 – Subglacial drainage characteristics – (**A**) Percent velocity changes along one of the inferred Nordenskiöld drainage pathways (black dashed line *Fig. 2*) as the velocity wave propagates to the margin (right to left). Stars show tracked wave peaks and circles show tracked wave fronts (*SI*). (**B**) Estimated wave velocity using the tracked peaks (stars) and fronts (circles). Velocity marker is shown at the mid-point between the two tracked peaks or fronts used to estimate the speed. Dashed bounds show event-integrated drainage velocity inferred from optical imagery (*Fig. S2*). (**C**) Left axis shows hydropotential (maroon line) assuming ice-overburden pressure, right-axis shows hydropotential gradients (black line), and smoothed hydropotential gradients (orange line) along flowline. Blue shading shows the location of hydropotential depressions.
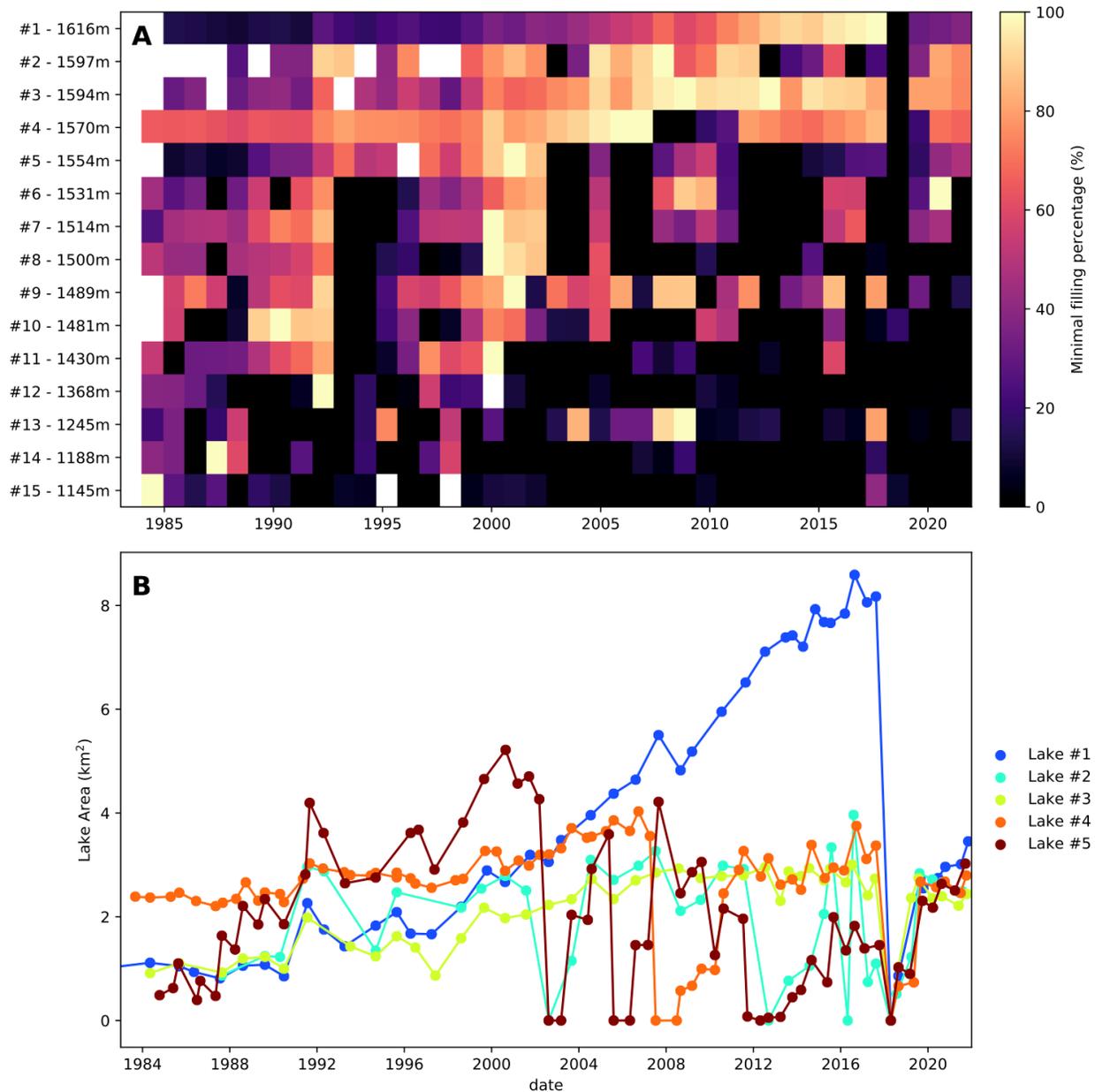
Figure 4 – Multi-decadal supraglacial lake evolution - (**A**) The percent fill of the lakes since 1983 relative to the largest area observed over the 1983-2022 period is shown. Where multiple areas are estimated for a year, the minimum value is shown, which generally indicates that the lake emptied in that year. The lake contours used to calculate the area are digitized from the Landsat archive (*SI*). The altitude of each lake is indicated next to the lake number. (**B**) The area of the five highest lakes in elevation as a function of time is plotted (all lakes shown in *Fig. S8*). We note Lake 1 could be identified all the way back to 1972.

Author Contributions: NM analyzed the data, identified the SGL drainages, and is the primary author of the manuscript. JKA produced the DInSAR time series and contributed to the writing of the manuscript. JM produced the historical SGL record and contributed to the data analysis and writing of the manuscript. FG contributed to the data analysis and writing of the manuscript. OG contributed to the writing of the manuscript. **Competing Interests:** The authors declare no competing interests.

References:

Andersen, J. K., Kusk, A., Boncori, J. P. M., Hvidberg, C. S., & Grinsted, A. (2020). Improved ice

velocity measurements with Sentinel-1 TOPS interferometry. *Remote Sensing*, *12*(12), 2014.

Andrews, L. C., Catania, G. A., Hoffman, M. J., Gulley, J. D., Lüthi, M. P., Ryser, C., et al. (2014).

Direct observations of evolving subglacial drainage beneath the Greenland Ice Sheet. *Nature*,

514(7520), 80.

Andrews, L. C., Hoffman, M. J., Neumann, T. A., Catania, G. A., Lüthi, M. P., Hawley, R. L., et al.

(2018). Seasonal evolution of the subglacial hydrologic system modified by supraglacial lake

drainage in western Greenland. *Journal of Geophysical Research: Earth Surface*, *123*(6), 1479–

1496.

Bartholomaus, T. C., Anderson, R. S., & Anderson, S. P. (2008). Response of glacier basal motion to

transient water storage. *Nature Geoscience*, *1*(1), 33–37. https://doi.org/10.1038/ngeo.2007.52

Bartholomew, I., Nienow, P., Mair, D., Hubbard, A., King, M. A., & Sole, A. (2010). Seasonal evolution

of subglacial drainage and acceleration in a Greenland outlet glacier. *Nature Geoscience*, *3*(6),

408–411.

Benedek, C. L., & Willis, I. C. (2021). Winter drainage of surface lakes on the Greenland Ice Sheet from

    Sentinel-1 SAR imagery. *The Cryosphere*, *15*(3), 1587–1606.

Chandler, D., Wadham, J., Lis, G., Cowton, T., Sole, A., Bartholomew, I., et al. (2013). Evolution of the

    subglacial drainage system beneath the Greenland Ice Sheet revealed by tracers. *Nature*

    Geoscience, *6*(3), 195–198.

Christoffersen, P., Bougamont, M., Hubbard, A., Doyle, S. H., Grigsby, S., & Pettersson, R. (2018).

    Cascading lake drainage on the Greenland Ice Sheet triggered by tensile shock and fracture.

    Nature Communications, *9*(1), 1–12.

Chudley, T. R., Christoffersen, P., Doyle, S. H., Bougamont, M., Schoonman, C. M., Hubbard, B., &

    James, M. R. (2019). Supraglacial lake drainage at a fast-flowing Greenlandic outlet glacier.

    Proceedings of the National Academy of Sciences, *116*(51), 25468–25477.

Cowton, T., Nienow, P., Sole, A., Bartholomew, I., & Mair, D. (2016). Variability in ice motion at a land-

    terminating Greenlandic outlet glacier: the role of channelized and distributed drainage systems.

    Journal of Glaciology, *62*(233), 451–466.

Das, S. B., Joughin, I., Behn, M. D., Howat, I. M., King, M. A., Lizarralde, D., & Bhatia, M. P. (2008).

    Fracture propagation to the base of the Greenland Ice Sheet during supraglacial lake drainage.

    Science, *320*(5877), 778–781.

Davison, B. J., Sole, A. J., Livingstone, S. J., Cowton, T. R., & Nienow, P. W. (2019). The influence of

    hydrology on the dynamics of land-terminating sectors of the Greenland Ice Sheet. *Frontiers in*

    Earth Science, *7*, 10.

Derkacheva, A., Gillet-Chaulet, F., Mouginot, J., Jager, E., Maier, N., & Cook, S. (2021). Seasonal

    evolution of basal environment conditions of Russell sector, West Greenland, inverted from

    satellite observation of surface flow. *The Cryosphere*, *15*(12), 5675–5704.

Dow, C. F., Werder, M. A., Nowicki, S., & Walker, R. T. (2016). Modeling Antarctic subglacial lake filling

    and drainage cycles. *The Cryosphere*, *10*(4), 1381–1393.

Doyle, S. H., Hubbard, A. L., Dow, C. F., Jones, G. A., Fitzpatrick, A. A. W., Gusmeroli, A., et al. (2013).
Ice tectonic deformation during the rapid in situ drainage of a supraglacial lake on the
Greenland Ice Sheet. *Cryosphere*, *7*(1), 129–140.

Gagliardini, O., Cohen, D., Råback, P., & Zwinger, T. (2007). Finite-element modeling of subglacial
cavities and related friction law. *Journal of Geophysical Research: Earth Surface*, *112*(F2).
https://doi.org/10.1029/2006JF000576

Gilbert, A., Gimbert, F., Thøgersen, K., Schuler, T. V., & Kääb, A. (2022). A Consistent Framework for
Coupling Basal Friction With Subglacial Hydrology on Hard-Bedded Glaciers. *Geophysical
Research Letters*, *49*(13), e2021GL097507.

Gimbert, F., Gilbert, A., Gagliardini, O., Vincent, C., & Moreau, L. (2021). Do Existing Theories Explain
Seasonal to Multi-Decadal Changes in Glacier Basal Sliding Speed? *Geophysical Research
Letters*, *48*(15), e2021GL092858.

Harper, J., Meierbachtol, T., Humphrey, N., Saito, J., & Stansberry, A. (2021). Generation and fate of
basal meltwater during winter, western Greenland Ice Sheet. *The Cryosphere*, *15*(12), 5409–
5421.

Helanow, C., Iverson, N. R., Woodard, J. B., & Zoet, L. K. (2021). A slip law for hard-bedded glaciers
derived from observed bed topography. *Science Advances*, *7*(20), eabe7798.

Hoffman, M., Catania, G. A., Neumann, T., Andrews, L., & Rumrill, J. (2011). Links between
acceleration, melting, and supraglacial lake drainage of the western Greenland Ice Sheet.
Journal of Geophysical Research: Earth Surface, *116*(F4).

Hoffman, M. J., Andrews, L. C., Price, S. F., Catania, G. A., Neumann, T. A., Lüthi, M. P., et al. (2016).
Greenland subglacial drainage evolution regulated by weakly connected regions of the bed.
Nature Communications, *7*, 13903.

Hoffman, M. J., Perego, M., Andrews, L. C., Price, S. F., Neumann, T. A., Johnson, J. V., et al. (2018).
Widespread moulin formation during supraglacial lake drainages in Greenland. *Geophysical
Research Letters*, *45*(2), 778–788.

Koenig, L. S., Lampkin, D., Montgomery, L., Hamilton, S., Turrin, J., Joseph, C., et al. (2015). Wintertime storage of water in buried supraglacial lakes across the Greenland Ice Sheet. *The Cryosphere*, *9*(4), 1333–1342.

Kusk, A., Boncori, J. P. M., & Dall, J. (2018). An automated system for ice velocity measurement from SAR (pp. 1–4). Presented at the EUSAR 2018; 12th European Conference on Synthetic Aperture Radar, VDE.

Kusk, A., Andersen, J. K., & Boncori, J. M. (2021). Sentinel-1 TOPS Interferometry for Ice Flow Mapping (pp. 1–5). Presented at the EUSAR 2021; 13th European Conference on Synthetic Aperture Radar, VDE.

Lampkin, D. J., Koenig, L., Joseph, C., & Box, J. E. (2020). Investigating controls on the formation and distribution of wintertime storage of water in supraglacial lakes. *Frontiers in Earth Science*, 370.

Law, R., Arnold, N., Benedek, C., Tedesco, M., Banwell, A., & Willis, I. (2020). Over-winter persistence of supraglacial lakes on the Greenland Ice Sheet: Results and insights from a new model. *Journal of Glaciology*, *66*(257), 362–372.

Leeson, A., Shepherd, A., Briggs, K., Howat, I., Fettweis, X., Morlighem, M., & Rignot, E. (2015). Supraglacial lakes on the Greenland ice sheet advance inland under warming climate. *Nature Climate Change*, *5*(1), 51–55.

Legleiter, C., Tedesco, M., Smith, L., Behar, A., & Overstreet, B. (2014). Mapping the bathymetry of supraglacial lakes and streams on the Greenland ice sheet using field measurements and high-resolution satellite images. *The Cryosphere*, *8*(1), 215–228.

Livingstone, S. J., Utting, D. J., Ruffell, A., Clark, C. D., Pawley, S., Atkinson, N., & Fowler, A. C. (2016). Discovery of relict subglacial lakes and their geometry and mechanism of drainage. *Nature Communications*, *7*(1), 1–9.

Maier, N., Humphrey, N., Meierbachtol, T., & Harper, J. (2021). Deformation motion tracks sliding changes through summer, western Greenland. *Journal of Glaciology*, 1–10.

Maier, N., Gimbert, F., & Gillet-Chaulet, F. (2022). Threshold response to melt drives large-scale bed weakening in Greenland. *Nature*, *607*(7920), 714–720.

Mejía, J., Gulley, J., Trunz, C., Covington, M., Bartholomaus, T., Xie, S., & Dixon, T. (2021). Isolated cavities dominate Greenland ice sheet dynamic response to lake drainage. *Geophysical Research Letters*, *48*(19), e2021GL094762.

Morin, P., Porter, C., Cloutier, M., Howat, I., Noh, M.-J., Willis, M., et al. (2016). ArcticDEM; a publically available, high resolution elevation model of the Arctic (pp. EPSC2016-8396). Presented at the Egu general assembly conference abstracts.

Morlighem, M. (2018). IceBridge BedMachine Greenland, Version 3. *Boulder, Colorado USA. NASA National Snow and Ice Data Center Distributed Active Archive Center*. https://doi.org/10.5067/2CIX82HUV88Y

Morlighem, M., Williams, C. N., Rignot, E., An, L., Arndt, J. E., Bamber, J. L., et al. (2017). BedMachine v3: Complete bed topography and ocean bathymetry mapping of Greenland from multibeam echo sounding combined with mass conservation. *Geophysical Research Letters*, *44*(21), 11–051.

Mouginot, J., Rignot, E., Bjørk, A. A., Van Den Broeke, M., Millan, R., Morlighem, M., et al. (2019). Forty-six years of Greenland Ice Sheet mass balance from 1972 to 2018. *Proceedings of the National Academy of Sciences*, *116*(19), 9239–9244.

Podolskiy, E. A., Fujita, K., Sunako, S., & Sato, Y. (2019). Viscoelastic Modeling of Nocturnal Thermal Fracturing in a Himalayan Debris-Covered Glacier. *Journal of Geophysical Research: Earth Surface*, *124*(6), 1485–1515.

Pope, A., Scambos, T. A., Moussavi, M., Tedesco, M., Willis, M., Shean, D., & Grigsby, S. (2016). Estimating supraglacial lake depth in West Greenland using Landsat 8 and comparison with other multispectral methods. *The Cryosphere*, *10*(1), 15–27.

Rada, C., & Schoof, C. (2018). Channelized, distributed, and disconnected: subglacial drainage under a valley glacier in the Yukon. *Cryosphere*, *12*(8).

Ryser, C., Lüthi, M. P., Andrews, L. C., Catania, G. A., Funk, M., Hawley, R., et al. (2014). Caterpillar-like ice motion in the ablation zone of the Greenland ice sheet. *Journal of Geophysical Research: Earth Surface*, *119*(10), 2258–2271.

Schoof, C. (2005). The effect of cavitation on glacier sliding. *Proceedings of the Royal Society A: Mathematical, Physical and Engineering Sciences*, *461*(2055), 609–627. https://doi.org/10.1098/rspa.2004.1350

Schröder, L., Neckel, N., Zindler, R., & Humbert, A. (2020). Perennial supraglacial lakes in Northeast Greenland observed by polarimetric SAR. *Remote Sensing*, *12*(17), 2798.

Sole, A., Nienow, P., Bartholomew, I., Mair, D., Cowton, T., Tedstone, A., & King, M. A. (2013). Winter motion mediates dynamic response of the Greenland Ice Sheet to warmer summers. *Geophysical Research Letters*, *40*(15), 3940–3944.

Solgaard, A., Kusk, A., Merryman Boncori, J. P., Dall, J., Mankoff, K. D., Ahlstrøm, A. P., et al. (2021). Greenland ice velocity maps from the PROMICE project. *Earth System Science Data*, *13*(7), 3491–3512.

Stevens, L. A., Behn, M. D., McGuire, J. J., Das, S. B., Joughin, I., Herring, T., et al. (2015). Greenland supraglacial lake drainages triggered by hydrologically induced basal slip. *Nature*, *522*(7554), 73–76.

Tedesco, M., Willis, I. C., Hoffman, M. J., Banwell, A. F., Alexander, P., & Arnold, N. S. (2013). Ice dynamic response to two modes of surface lake drainage on the Greenland ice sheet. *Environmental Research Letters*, *8*(3), 034007.

Tsai, V. C., & Rice, J. R. (2010). A model for turbulent hydraulic fracture and application to crack propagation at glacier beds. *Journal of Geophysical Research: Earth Surface*, *115*(F3).

Tsai, V. C., Smith, L. C., Gardner, A. S., & Seroussi, H. (2022). A unified model for transient subglacial water pressure and basal sliding. *Journal of Glaciology*, *68*(268), 390–400.

Van de Wal, R., Smeets, C., Boot, W., Stoffelen, M., Van Kampen, R., Doyle, S. H., et al. (2015). Self-regulation of ice flow varies across the ablation area in south-west Greenland. *Cryosphere*, *9*(2), 603–611.

Vandecrux, B., MacFerrin, M., Machguth, H., Colgan, W. T., As, D. van, Heilig, A., et al. (2019). Firn data compilation reveals widespread decrease of firn air content in western Greenland. *The Cryosphere*, *13*(3), 845–859.

Supporting Info for

Wintertime lake drainage cascade triggers large-scale ice flow response in Greenland

Authors:

Nathan Maier[1,2]*, Jonas Kvist Andersen[3], Jeremie Mouginot[1,4], Florent Gimbert[1] and Olivier Gagliardini[1]

Affiliations:

[1]Univ. Grenoble Alpes, CNRS, IRD, Grenoble INP, IGE, 38000 Grenoble, France

[2]Los Alamos National Lab, Los Alamos, NM 87544,USA

[3]DTU Space, Tech. Univ. of Denmark, 2800 Kgs. Lyngby, Denmark

[4]Depart. of Earth System Science, Univ. of California- Irvine, Irvine CA 92697, USA

*Corresponding Author Email: ntmaier@gmail.com

Supporting Information

1 Supporting Methods

1.1 DInSAR Velocities and Annual Impact

To process the interferograms, the 2016-2019 multi-year average velocity map was generated through PROMICE (Solgaard et al., 2021) and the TanDEM-X Digital Elevation Model were used for image coregistration and phase flattening respectively. Interferograms are multi-looked with a factor of 15 x 3 in range/azimuth and unwrapped using a Minimum Cost Flow algorithm. The resulting 6-day LoS velocity maps have a pixel spacing of 50 m x 50 m and measurements from all tracks are resampled to the same (50 m x 50 m) grid. The DTU IPP software (Kusk et al., 2018) is used for all interferometric processing steps.

In some cases, we use flow-projected velocities where LoS measurements are projected onto the flow direction obtained by the 2016-2019 multi-year average velocity map (Solgaard et al., 2021), assuming that all motion is horizontally derived. This is used to compare the increased displacement resulting from the winter drainage to the multi-year average velocity (*Fig. S9*) to estimate the effect the event had on annual dynamics. We note we use the multiyear velocity average instead of using the full 2018 annual velocity series because the later cannot be resolved using DInSAR due to decorrelation during summer. Thus, this reflects increased displacement of the drainage event compared to a "typical year" average velocity. Because the flood wave causes uplift and downlift as it moves into a region and then passes, the integrated displacement of the flow projected velocities will mostly reflect horizontal motion.

1.2 Estimating Approximate SGL Volumes

Depth retrieval based on empirical (Legleiter et al., 2014) or physical (Pope et al., 2016) multi-spectral methods cannot be applied to estimate SGL volumes due to the presence of an ice lid during winter. Examining the near 50-year time series (described below) also shows that many of the high elevation lakes never become ice-free even during summer. To circumvent these limitations and roughly estimate total SGL volume prior to drainage we interpolate the sub-lake bathymetry from 2 m resolution ArcticDEMs (Morin et al., 2016). We start by manually digitizing each lake-outline along the visible edge of the ice lid and remove this area from a corresponding ArcticDEM strip collected between 2013 and 2017 during times where the lake volume is inferred to be lower or similar to that during the 2018 winter. We then interpolate a lake bathymetry using a spline (MATLAB curve fitting toolbox, smoothing parameter 0.9) over seven SGL cross sections (*Fig. S12*). The fit relies on the local slope adjacent to the ice basin to estimate the lake depth (*Fig. S13*). The maximum lake depths agree well with those found by other methods (~4-10 m) (Legleiter et al., 2014; Pope et al., 2016). The ice lid elevation is estimated using the median of the intersecting points between the lake outline and the DEM. We can then estimate the lake volume by assuming a lid thickness of ~2 m which has been observed (Lampkin et al., 2020) and modeled (Law et al., 2020) at the end of winter and then integrate the volume at each DEM grid cell. We note that even though the method has high uncertainty, it overcomes the limitations of winter imagery while still being empirically based. We test the sensitivity of the volume estimates by repeating the procedure using 8 different DEMs for Lake 2 and show a consistency of +/- 11%. We note most of the lakes are identified with collapsed ice lids, such that actual volume of water that makes it to the bed cannot be confidently estimated, as some of the lakes may have only partially drained. Thus, we interpret these estimates as rough volume maximums which could have drained to the bed.

1.3 Interpreted Drainage Pathways

The decomposed velocity components demonstrate that the complex structure is a result of vertical uplift (*Fig. 2*) which were interpreted to represent primary drainage pathways. Using this interpretation, we manually delineate the major flow pathways using a map of the maximum LoS velocities recorded during the event, which retains the complex structure from the drainage site to the margin (*Fig. S4*). Two major westward pathways, one major northward drainage pathway, a secondary drainage pathway from the lake drainages that occur just upgradient of the Nordenskiöld trough, and a connector between the secondary and primary westward drainage pathways are identified.

1.4 Drainage Velocities

We track the wave front and peaks for consecutive DInSAR velocity maps (using track T90) to determine the position of the velocity wave through time along inferred drainage pathways. The wave front is defined as the first location on the ascending limb of the wave where LoS velocities are 10% higher than pre-drainage velocities. The wave peak is taken as the flowline maximum. We then differentiate the wave fronts or peaks between two consecutive flowline velocity profiles to get the distance traveled which is converted to velocity using the 6-day repeat period (*Fig. 3*).

1.5 Long-term SGL Evolution

We document the evolution of the surface area for the 15 supraglacial lakes identified to drain during the event over the last 50 years. We downloaded 1275 optical images from the Landsat satellite record that began in 1972 (only 1983 onward is shown in *Fig. 4*), built a stack of sub-images for each lake and manually digitized their outline twice a year when possible, before May/June when the melt season begins and a second time between August and November at the end of the melt season. We then calculated the evolution of the area of the lakes (*Fig. 4*) through time to establish the historical context of the SGL evolution preceding the winter drainage event.
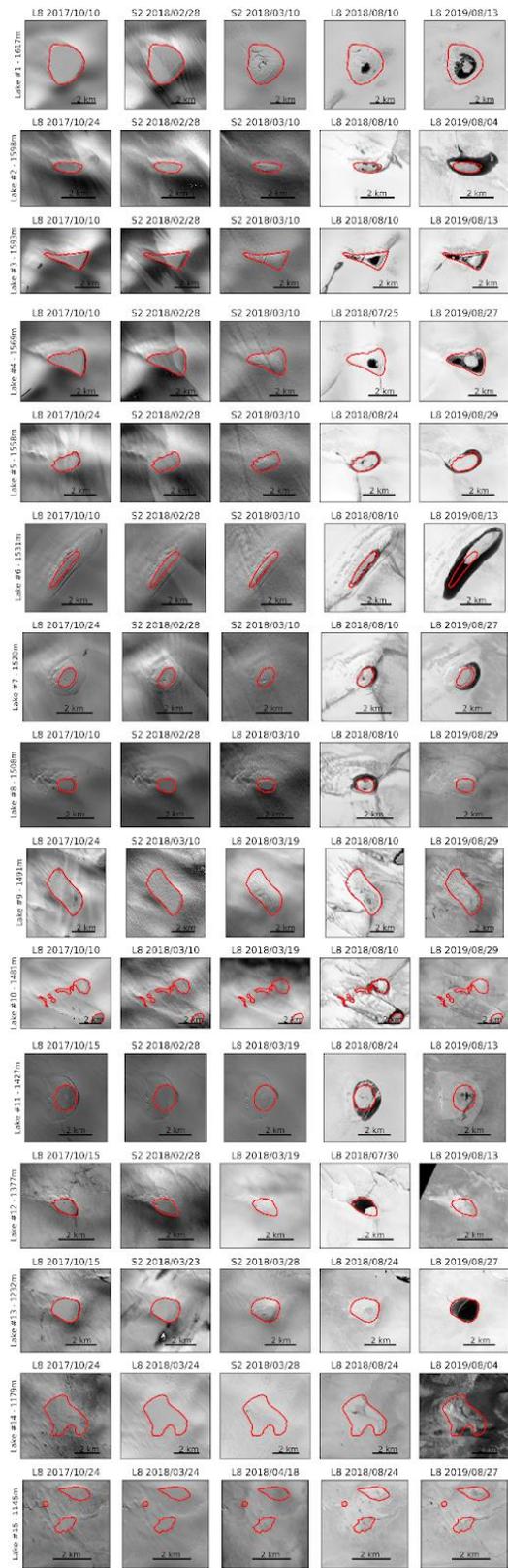
Figure S1 - Lake evolution before and after the drainage from Landsat (L8) and Sentinel-2 (S2) optical images. The red outlines indicate the lake perimeters in fall 2017 prior to the event.
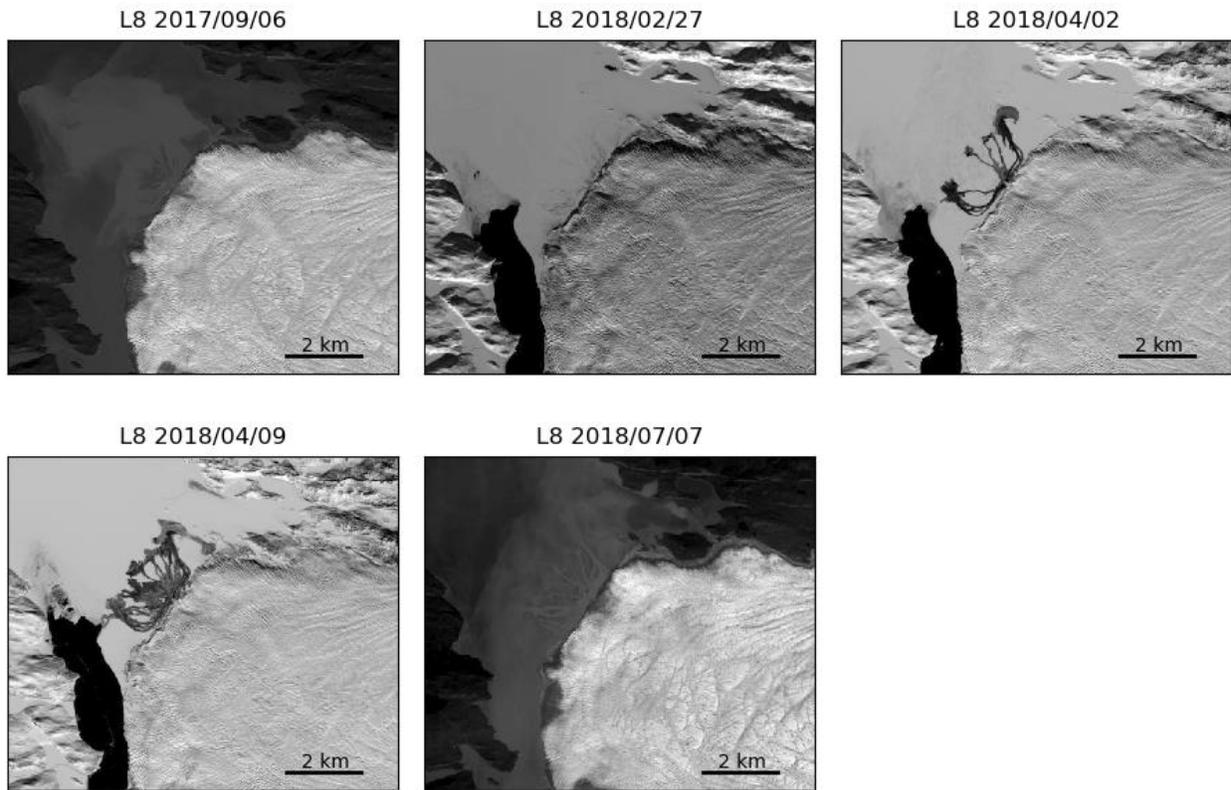
Figure S2 – Landsat images of the Nordenskiöld ice tongue showing the outwash in early April 2018 following supraglacial lake drainages. At this time of the year the surface of the sedimentary delta in front of Nordenskiöld is covered with snow, making it possible to clearly identify the areas swept by the flow.
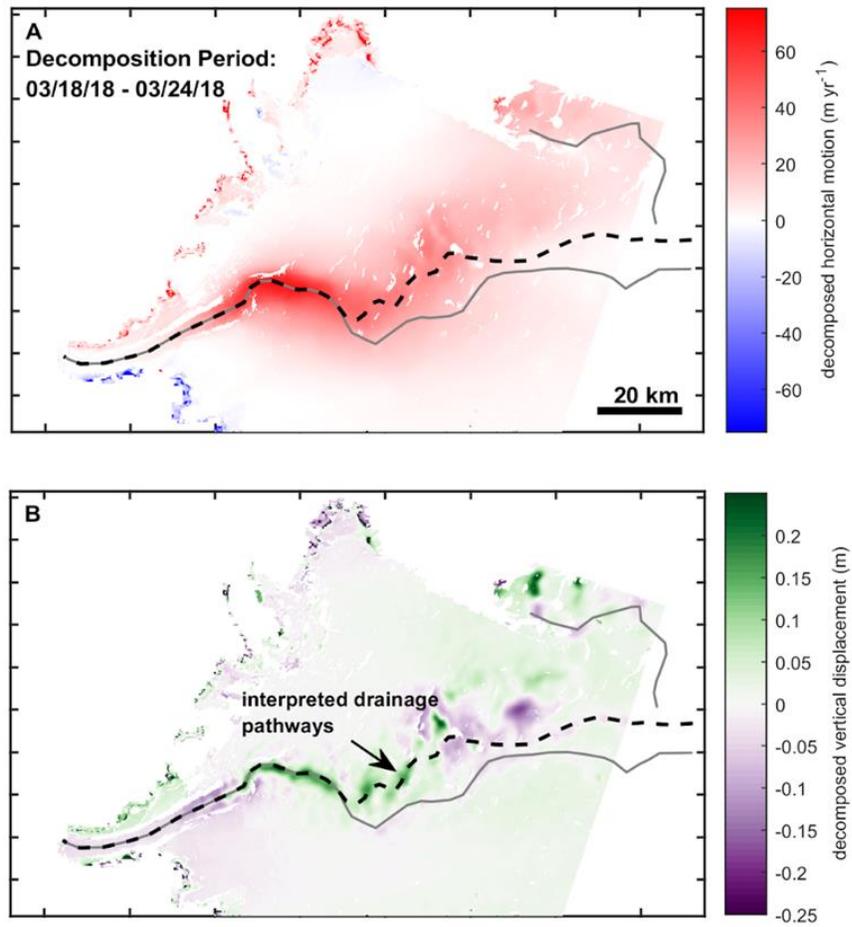
Figure S3 – Decomposed motion – Snapshot (03/18/18 - 3/24/18) of decomposed horizontal motion (relative to pre-drainage velocities) (**A**) and vertical surface displacement (**B**) during drainage event. This snapshot follows that presented in Figure 2.
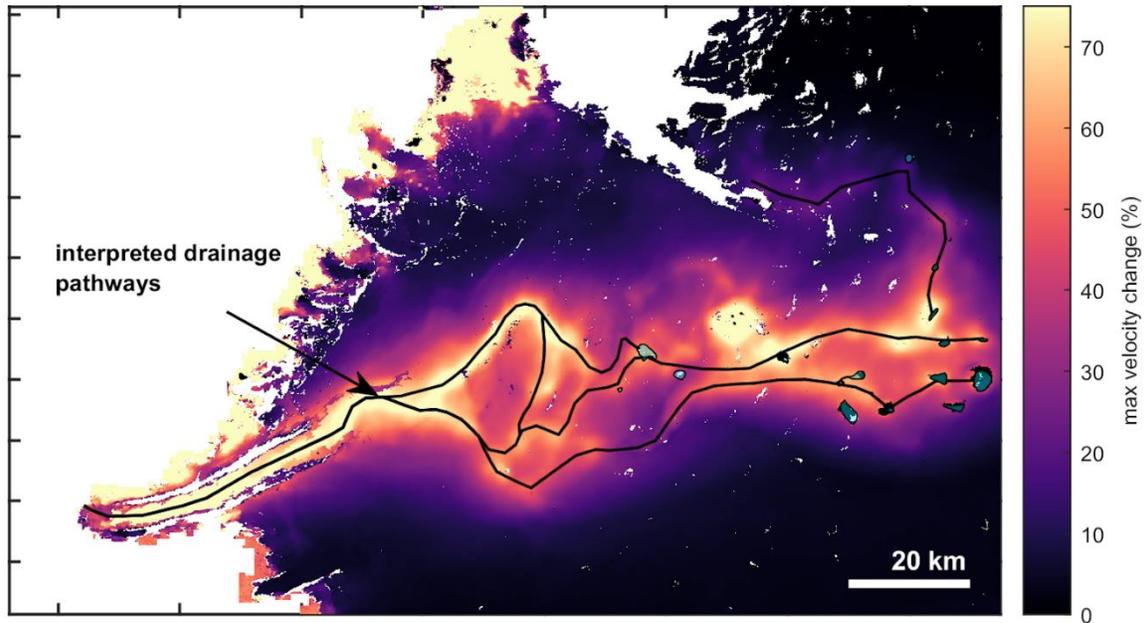
Figure S4 – Interpreted Drainage Pathways – Complex structure from max flow projected velocities during drainage event (Track 90) were used to visually interpret inferred drainage pathways (black lines). Cyan fill shows drained lake locations.
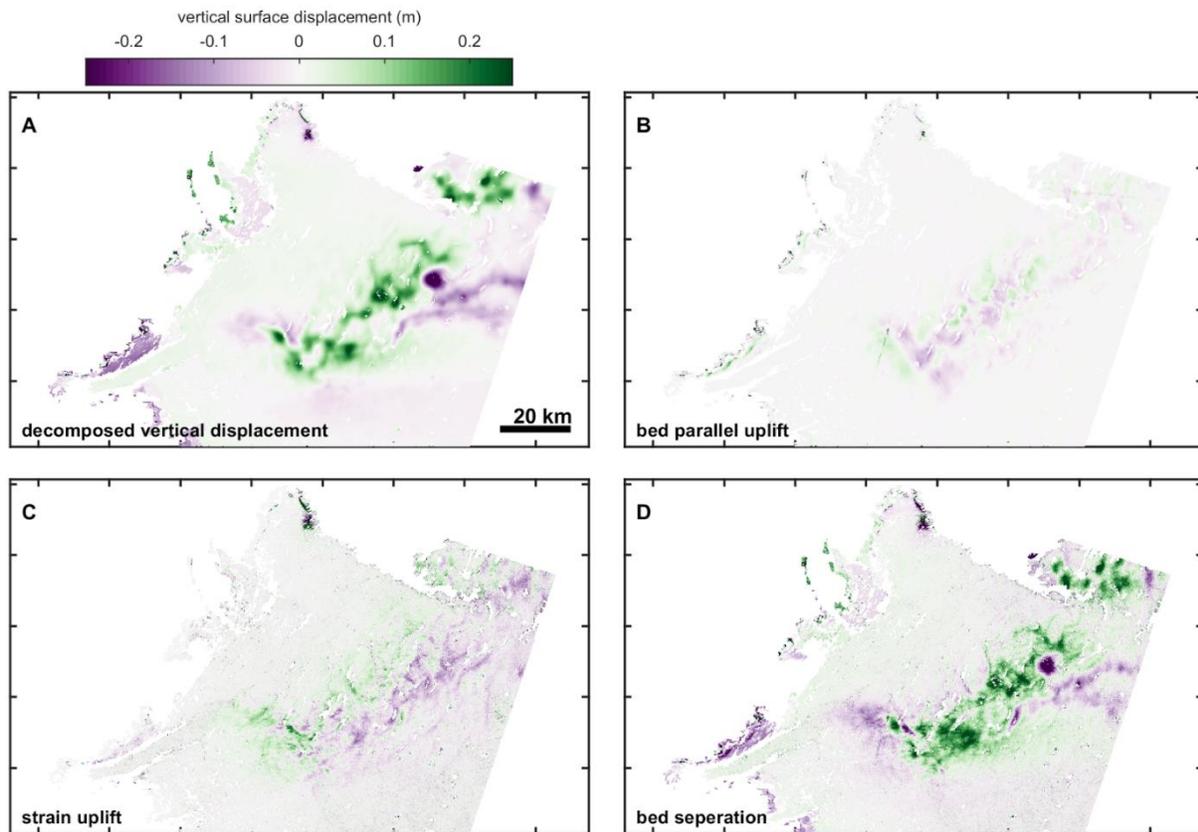
Figure S5 – Vertical surface displacement components – Decomposed vertical motion during drainage event (centered around 10.6 days after initial drainage using Track 90 and 25 velocities spanning from March, same as Fig. 2 in the main text) (**A**), bed parallel uplift (**B**), vertical displacement due to vertical strain (**C**), and bed separation (**D**). Vertical strain and bed parallel uplift were estimated with the decomposed horizontal velocity assuming changes in motion are derived from sliding. Bed separation is taken as the residual between the decomposed vertical motion and the bed parallel and vertical strain uplift.
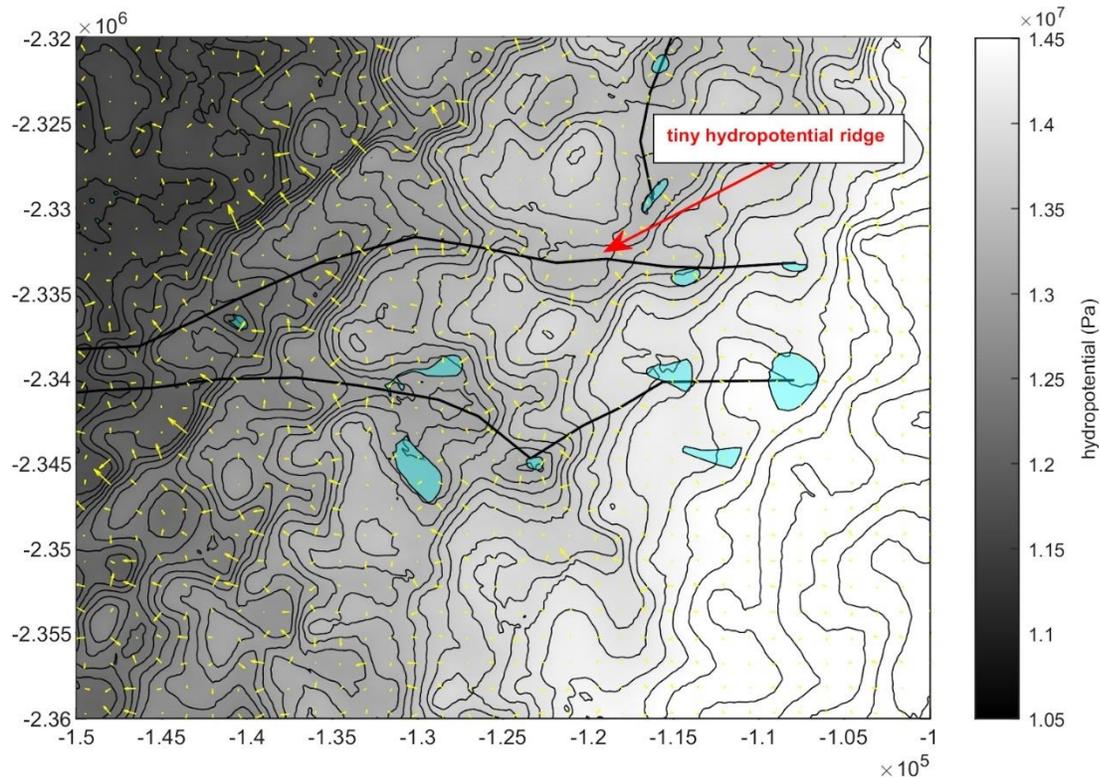
Figure S6 – Zoom of hydropotential for a region that incorporates the start of three major inferred drainage pathways. The two westward propagating drainage pathways are separated from the northernmost hydropotential pathway by a small ridge of high pressure (arrow). Hydropotential gradients were calculated assuming ice overburden pressure and hydropotential gradients (yellow vectors). Cyan regions show locations of supraglacial lakes that drained during the event. Contours of hydropotential (black lines) spaced 150 kPA apart are presented to better show troughs and ridges in the hydropotential field.
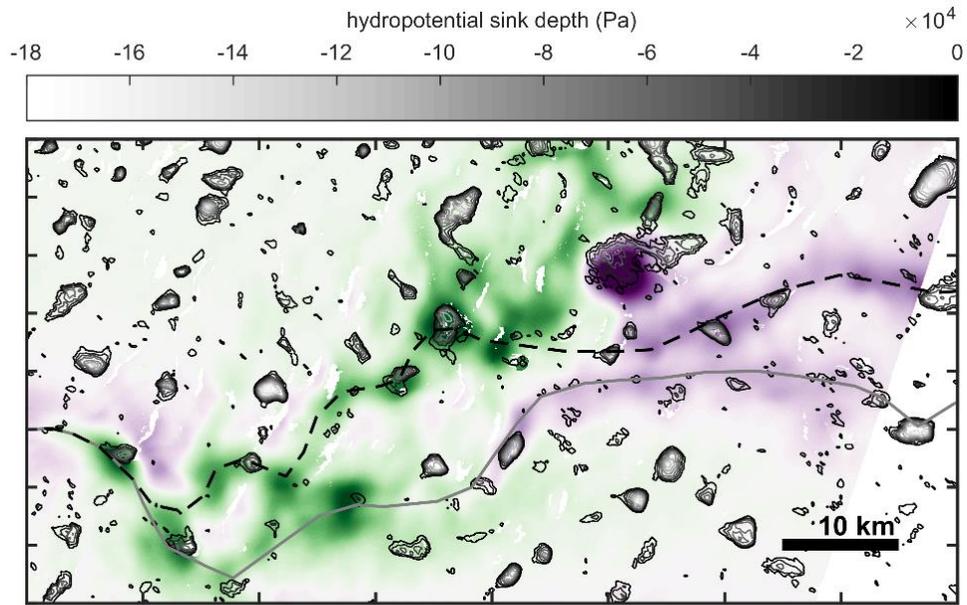
Figure S7 – Bead and thread uplift structure in relation to subglacial sinks and interpreted flowlines (same as shown on Fig. 2). Subglacial sinks are delineated with hydropotential contours calculated assuming ice overburden pressure.
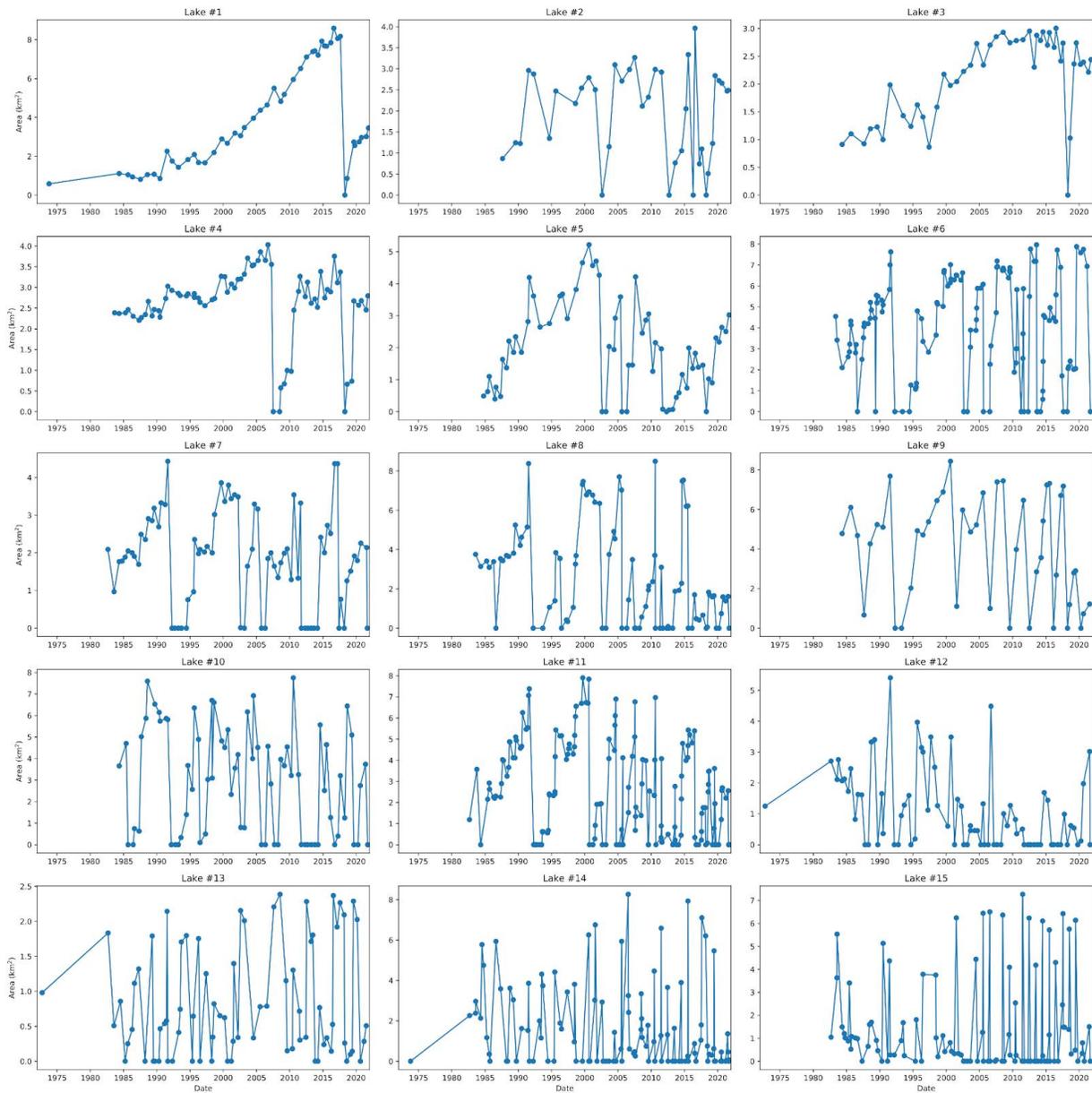
Figure S8 – The area of lakes that drained during the event is plotted as a function of time.
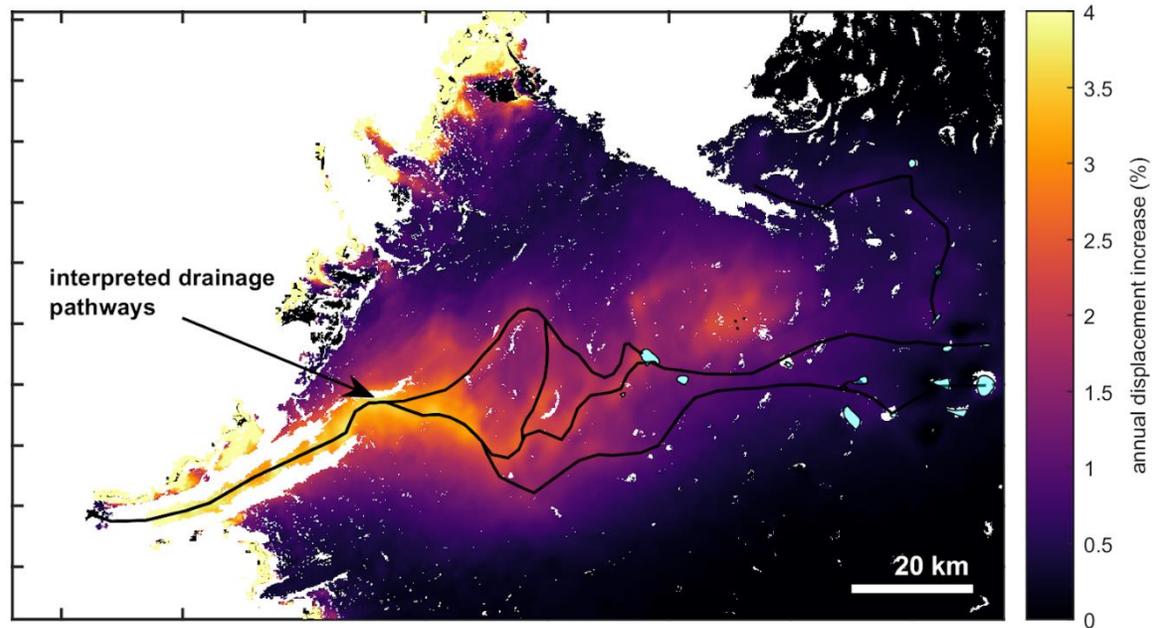
Figure S9 – Percent increase in annual velocity due to elevated velocities during the event. Black lines show inferred flow pathways. Increase was calculated using multi-year average annual displacement from 2016-2019 (Solgaard et al., 2021) and comparing it to increased displacement during the drainage event (*SI*).
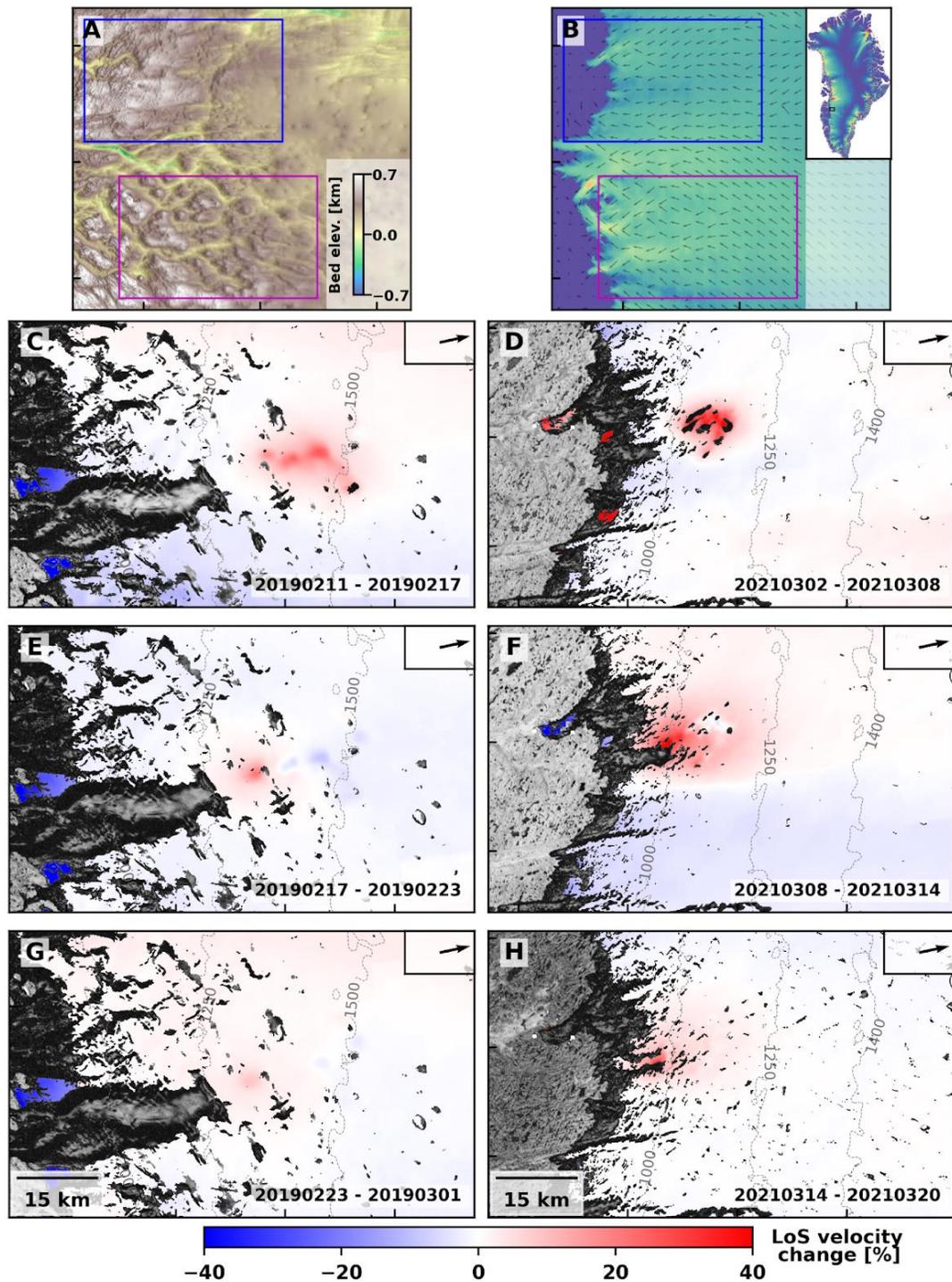
Figure S10 – Dynamic response to lake drainages identified during February 2019 40 km south of Russell Glacier (**C**,**E**,**G**) and March 2021 50 km north of Russell Glacier (**D**,**F**,**H**) measured with Sentinel-1 DInSAR (track 90) consecutive 6-day pairs. Panels (**C**)-(**H**) show the relative change in line-of-sight velocity (in percent) with respect to a pre-event acquisition overlayed on the coherence for the respective image pair. Panels (**A**) and (**B**) show bed elevation and 1995-2016 average velocity in the region of the 2019 event (magenta rectangle) and the 2021 event (blue rectangle).
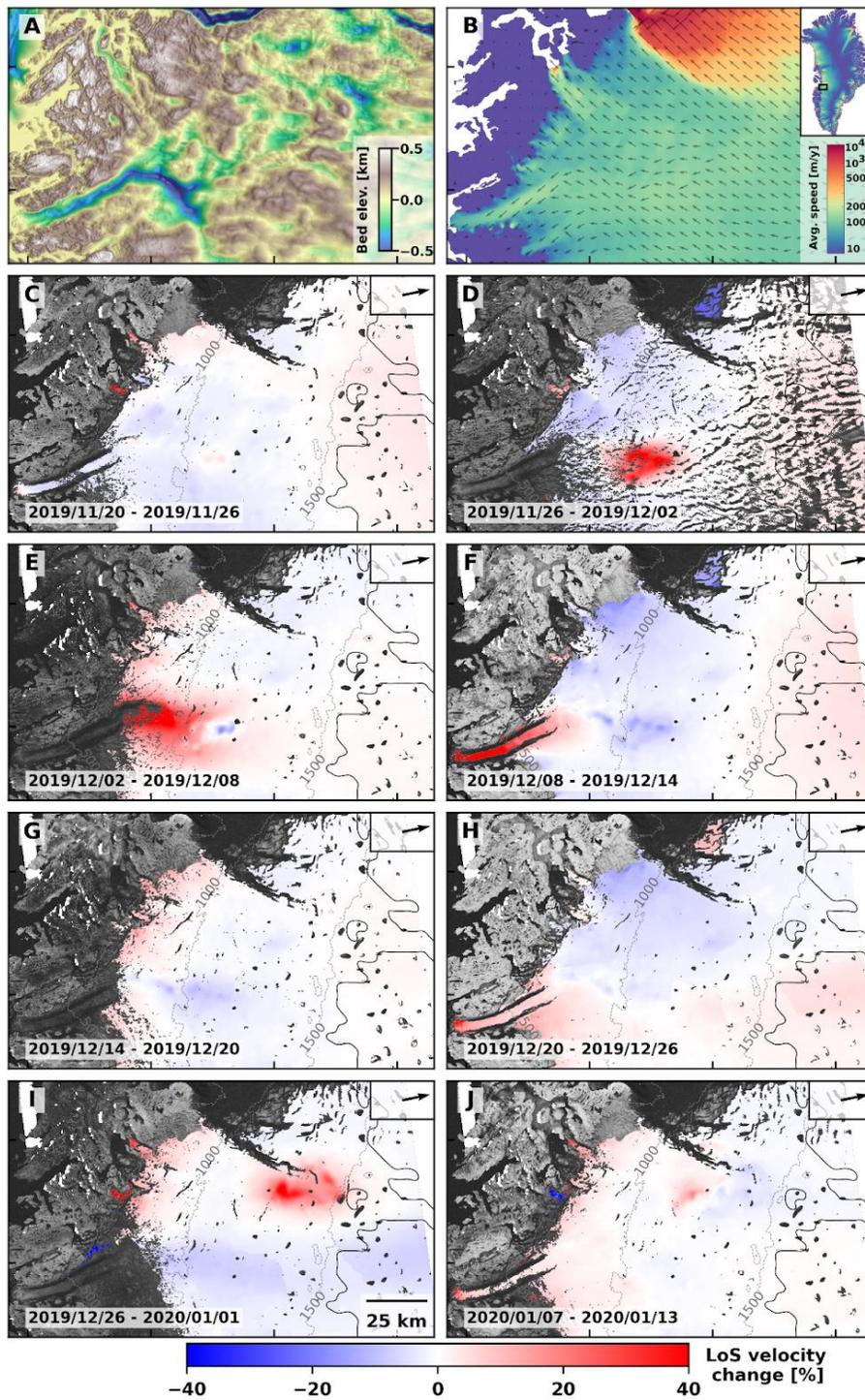
Figure S11 – Dynamic response to two additional lake drainages identified during early December 2019 (**C**,**E**,**F**) and late December 2019 (**H, I, J**) measured with Sentinel-1 DInSAR (track 90) consecutive 6-day pairs. Panels (**C**)-(**H**) show the relative change in line-of-sight velocity (in percent) with respect to a pre-event acquisition overlayed on the coherence for the respective image pair. Panels (**A**) and (**B**) show bed elevation and 1995-2016 average velocity in the region of the 2019 event.
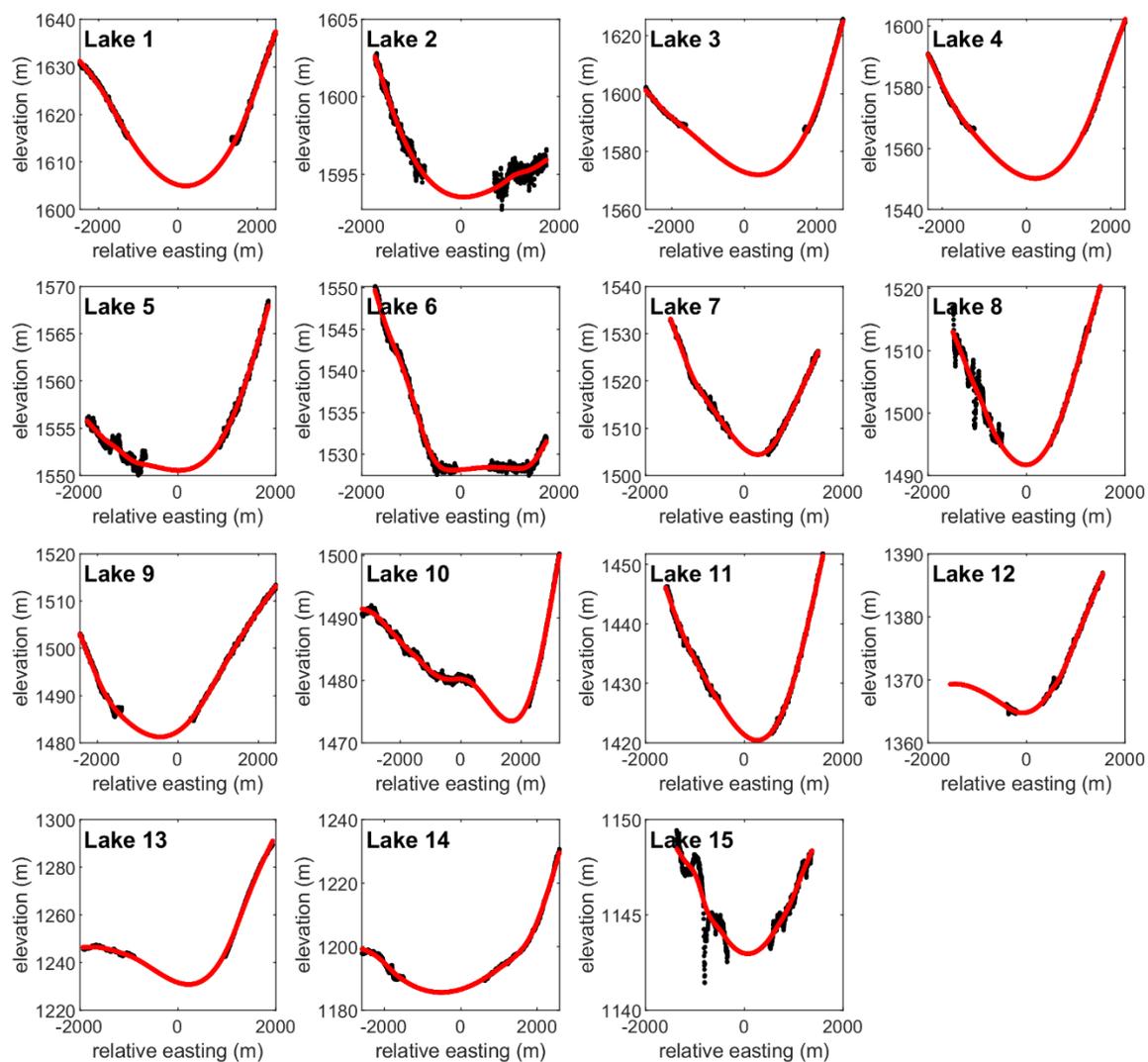
Figure S12 – Spline lake-bottom interpolation. Two-dimensional cross section of smoothing spline (red line, smoothing parameter = 0.9) fit through ArcticDEM (Morin et al., 2016) elevation data (black line) for all 15 lakes.
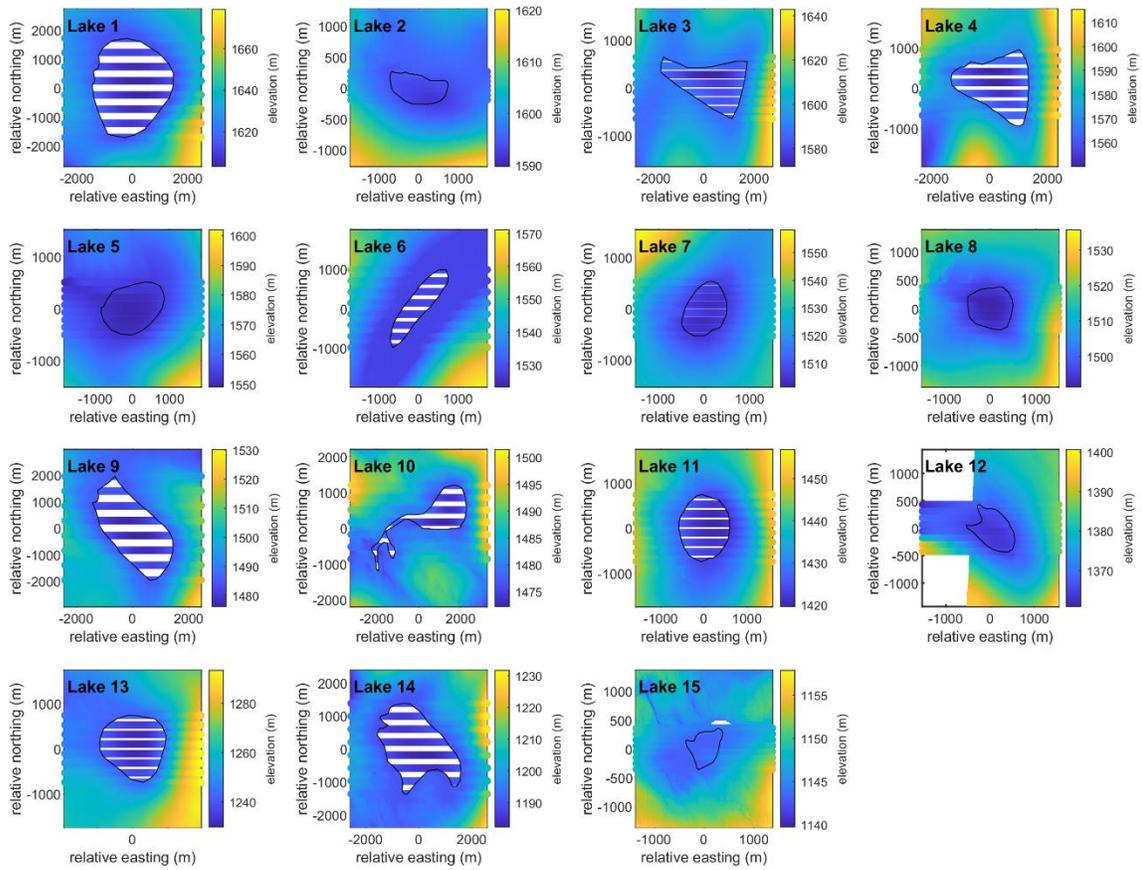
Figure S13 – Map view of spline lake-bottom interpolation. Map view of smoothing splines (horizontal lines, smoothing parameter = 0.9) fit through ArcticDEM (Morin et al., 2016) elevation data (background data) for all 15 lakes.